INSTITUTE OF PHYSICS PUBLISHING JOURNAL OF MICROMECHANICS AND MICROENGINEERING

J. Micromech. Microeng. **16** (2006) S182–S190 doi:10.1088/0960-1317/16/9/S03

Microball-bearing-supported electrostatic micromachines with polymer dielectric films for electromechanical power conversion

A Modafe[1], N Ghalichechian[1], A Frey[1], J H Lang[2] and R Ghodssi[1]

[1] MEMS Sensors and Actuators Lab (MSAL), Department of Electrical and Computer Engineering, The Institute for Systems Research, University of Maryland, College Park, MD 20742, USA

[2] Department of Electrical Engineering and Computer Science, Massachusetts Institute of Technology, Cambridge, MA 02139, USA

E-mail: ghodssi@eng.umd.eud

Received 8 March 2006, in final form 17 May 2006
Published 9 August 2006
Online at stacks.iop.org/JMM/16/S182

Abstract

This paper presents our latest research activities toward the development of electrostatic micromotors/microgenerators with a microball-bearing support mechanism and benzocyclobutene (BCB) low-k polymer insulating layers. The primary applications of these devices are long-range, high-speed micropositioning, high-speed micro pumping and micro power generation. In this paper, we present the development of the first generation of microball-bearing-supported micromachines. This device is a 6-phase, bottom-drive, linear, variable-capacitance micromotor. The design and fabrication of the linear micromotor, and characterization of the motor capacitance, force and motion in 3-phase and 6-phase excitation modes are presented. The micromotor consists of a silicon stator, a silicon slider and four stainless-steel microballs. The aligning force profile of the micromotor was extracted from simulated and measured capacitances of all phases. An average total aligning force of 0.27 mN with a maximum of 0.41 mN at 100 V dc was measured. The ac operation of the micromotor was verified by applying square-wave voltages and characterizing the slider motion. An average slider speed of 7.32 mm s^{-1} at 40 Hz and 120 V P-P was reached without losing the synchronization. The design, fabrication and characterization methods presented in this paper can be used as a technology platform for developing rotary micromachines.

(Some figures in this article are in colour only in the electronic version)

1. Introduction

Electric micromotors and microgenerators based on microelectromechanical systems (MEMS) technology are promising candidates to replace bulky sources of mechanical and electrical power in a variety of microsystem applications. However, reliability and efficiency of power microelectromechanical devices, such as micromotors and microgenerators have yet to reach their macroscale counterparts. Furthermore, the demand for higher power density in microsystems and portable electronics has pushed the standards to higher levels. In an effort to address these needs, we have developed an electrostatic microactuator that integrates two key enabling technologies: microball bearings in silicon [1] and thick low-dielectric-constant (low-k) benzocyclobutene (BCB) polymer insulating layers [2].

The first demonstration of this device is a 6-phase, bottom-drive, linear, variable-capacitance micromotor (B-LVCM) [3],

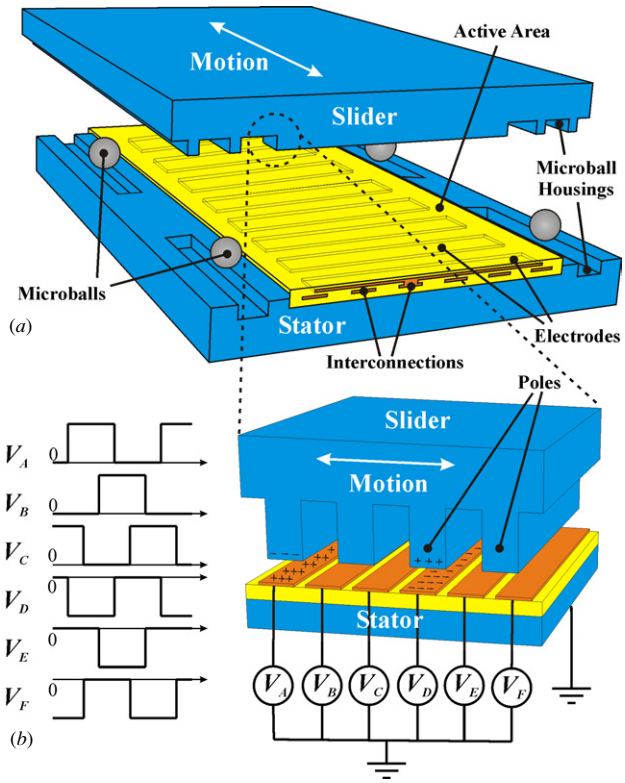

Figure 1. (*a*) Schematic 3D view of the 6-phase, bottom-drive, linear, variable-capacitance micromotor, and (*b*) principle of operation and square-wave excitation.

as shown in figure 1. The B-LVCM has been designed, fabricated and tested on the basis of our previous work on characterization and modeling of microball bearings [4–7], and characterization and process integration of BCB polymers [8–11]. The primary application of the B-LVCM is long-range, high-speed, linear micropositioning. Furthermore, it provides a technology platform for the development of reliable, efficient, rotary, electrostatic micromotors/microgenerators.

Microball bearings in silicon is an alternative technology to previously developed center-pin [12, 13], flange [12] and gas-lubricated [14] bearings. This technology has several advantages such as relatively simple mechanism, rolling motion with low friction and wear, stable and robust support for moving parts (e.g. rotor) and precise definition of the machine air gap (e.g. the gap between stator electrodes and rotor poles).

Thick low-k BCB polymers can replace silicon dioxide dielectric films to reduce the parasitic capacitance of the insulating layers, leading to lower electrical energy loss. Furthermore, they exhibit lower residual stress resulting in reduced wafer bow and improved uniformity of the machine air gap.

There are several types of micromotors, in which the electromechanical energy conversion is controlled by electric fields. They can be divided into two general categories: electro(quasi)static and elastodynamic. The major distinguishing feature of different types of electro(quasi)static micromotors in most cases is the structure of the moving component (i.e. rotor or slider), which defines the mechanism of charge distribution [15]. Table 1 lists common types of

Table 1. Types of electro(quasi)static micromotors.

Micromotor	Mechanism of charge distribution
Variable capacitance	Pole saliency (electrostatic)
Induction	Charge relaxation (electroquasistatic)
Permanent electret	Embedded fixed charge (electrostatic)
Corona discharge	Microionization (electrostatic)
Dielectric hysteresis	Hysteresis in polarization (electrostatic)
Solid-filled gap	Rolling petals on solid dielectric or ferroelectric (electrostatic)

electro(quasi)static micromotors and the mechanism of charge distribution in each of them [16–18].

The simple structure of the rotor in a variable-capacitance micromotor provides two major advantages over alternative micromotors: better accuracy in controlling the fabrication tolerances and higher reliability of the fabricated device. The variable-capacitance micromotor can provide an output power, torque/force and energy efficiency comparable to that of the other types of electro(quasi)static micromotors with the exception of elastodynamic and solid-filled gap micromotors.

Solid-filled gap micromotors are based on the concept of scratch-drive actuators [19] where the gap between the stator and the rotor poles (or petals) consists of a high-dielectric-constant thin film, e.g. a ferroelectric material [20]. By increasing the capacitance of the machine, the capacity of energy transfer of solid-gap micromotors increases remarkably. However, this advantage is obtained at the expense of energy efficiency, since the dissipated energy is a direct function of the machine capacitance. In these machines, the rotor thrust is generated by the elastic forces of the stretched petals, which are electrostatically anchored to the stator. As a result of physical contact and sliding motion of the rotor, the petals, the thin film and the rotor support guides are prone to wear, which can lead to reliability issues, e.g. mechanical and/or electrical failure.

Elastodynamic micromotors operate on the basis of the ferroelectric effect, where in most cases the rotor thrust is generated by frictional forces rather than electrostatic forces. Two common types are piezoelectric [21] and ultrasonic [22] motors. Generally speaking, elastodynamic micromotors have higher torque, but they suffer from wear and lower speed. Furthermore, fabrication of ferroelectric thin films and their integration with conventional microfabrication processes still present difficult challenges.

In this paper, we present the latest results of our work on the development of the first microball-bearing-supported micromotor. An overview of BCB polymers and their application in the B-LVCM and the detailed design of the device including design and control parameters are presented. We then present the fabrication process of the B-LVCM. Finally, the test and characterization results are presented.

2. Polymer dielectric films for MEMS

Traditionally, silicon dioxide films have been and still are used for isolation, interlayer dielectric and passivation in microelectronics and MEMS. Recent advances in the area of power MEMS [23, 24] include a significant number of research activities on the development of crack-free, low-stress, thick silicon dioxide films [25–30]. In addition to

electrical insulation, thick silicon dioxide films have been used for high-frequency [31] and thermal [32, 33] isolation. The drawbacks of silicon dioxide as an insulating film for MEMS applications include high dielectric constant, limited thickness due to high residual stress and high-temperature process. These limitations affect the performance, efficiency and reliability of the final device [10].

BCB polymers have several advantages over silicon dioxide for a variety of applications including electrical and thermal isolation in MEMS. These polymers were primarily used as ILD films for microelectronic applications [2], and more recently for low-temperature adhesive wafer bonding [34] and as structural materials [35] in MEMS. BCB polymers are commercially available in the form of partially-cured BCB monomers in a mesitylene solvent under a trademark name, Cyclotene^{TM}, from The Dow Chemical Company (Midland, MI).

Compared to silicon dioxide, the lower dielectric constant of BCB polymers ($k = 2.65$) leads to lower parasitic capacitances, and as a result, lower electrical energy loss in electrostatically-driven MEMS. The higher volume resistivity of BCB polymers ($\rho = 10^{19}\ \Omega$ cm) reduces the leakage current through the insulating layers. The thermal conductivity of BCB polymers ($\kappa = 0.29$ W m^{-1} K^{-1}) is five times smaller than that of silicon dioxide, making BCB a much better thermal insulator. Furthermore, the residual stress of BCB polymer films is one order of magnitude smaller than that of silicon dioxide. This allows the usage of very thick BCB polymer films with little concern about wafer bow and film crack, which are the major problems in application of thick silicon dioxide films. In addition, the deposition process of BCB polymers includes simple spin-coating and low-temperature curing, compared to more complicated and more expensive deposition techniques for silicon dioxide. Although the glass transition temperature of BCB polymers ($T_g = 350\ ^\circ$C) is much lower than the melting point of silicon dioxide ($T_m = 1710\ ^\circ$C), they can be used in a variety of low- to moderate-temperature applications in MEMS. BCB polymers are prone to moisture uptake, which can affect their physical properties. We have experimentally shown that the dielectric constant of BCB polymers does not change appreciably with moisture uptake, while their current–voltage characteristics (e.g. leakage current and breakdown voltage) are degraded [10]. Therefore, careful design of interconnections and dielectric layers is necessary to avoid breakdown in BCB-based high-voltage devices operating in an open environment.

Integration of BCB polymer films with conventional MEMS processes such as silicon bulk micromachining is not a trivial task, mainly because the polymer cannot withstand the harsh condition of some chemical environments (e.g. hot potassium hydroxide, KOH), and also because the adhesion of the polymer to inorganic films (e.g. metals) is poor. Thin BCB polymer film (of the order of 1 μm) has been successfully integrated with micromachined silicon v-grooves [8], while integration of thick BCB polymer films (of the order of 20 μm to 30 μm) is still facing difficult challenges, such as polymer undercut.

In order to integrate thick BCB polymer films with microball-bearing silicon structures, we have developed the embedded BCB in silicon (EBiS) process [11]. EBiS takes advantage of the unique features of thick BCB polymer films for electrical and thermal isolation and makes it possible to integrate these films with other microfabricated structures and devices. The objective of the EBiS process is to develop planarized isolated islands of thick BCB polymer film embedded in a silicon substrate. Each island acts as an insulating bed for the active area of a micromotor, where a two-level interconnection is fabricated [9]. The EBiS process is adopted from thick buried oxide in silicon (TBOS) process [27], which was developed to create isolated islands of plasma-enhanced chemical vapor deposited (PECVD) silicon dioxide to reduce the overall wafer bow for subsequent wafer bonding. EBiS, however, enables the incorporation of spin-on, thick BCB polymer films in silicon substrate, leading to excellent electrical and thermal isolation, lower electrical energy loss, lower residual stress and wafer bow, and easier fabrication and process integration.

3. Linear micromotor design

The B-LVCM, shown schematically in figure 1(*a*), consists of two silicon plates, stator and slider and four stainless-steel microballs. The slider is free to move and supported on the microballs (~285 μm in diameter) housed in 290 μm wide parallel trenches etched in both silicon plates. The depths of these trenches define the machine air gap. The microball housings on each side of the stator active area consist of two identical separate trenches to prevent jamming and collision of the microballs. In contrast to the stator, the housings on each side of the slider active area are continuous trenches so that the maximum range of motion is achieved.

The stator active area consists of a stack of five layers: (1) an insulating BCB layer that is formed by the EBiS process and electrically isolates the active area from the substrate, (2) a metal layer that forms six parallel interconnection lines, (3) an ILD BCB layer that electrically isolates the interconnection lines from electrodes, (4) a metal layer that forms several parallel electrodes, and (5) a passivation BCB layer that protects the active area. Each interconnection line connects every sixth electrode together to form a 6-phase motor. The slider active area consists of a salient silicon pole structure, which is formed by periodic parallel deeply-etched trenches. The slider active area is smaller (about 2/3) than the stator active area so that the size of the effective active area (where the electrostatic force is applied) is constant and equals the size of the slider active area. This also helps us to reduce the end effects caused by the fringing electric fields. The stator electrode pitch is designed to be different from the slider pole pitch so that the electrode to pole ratio is 3:2 (or 6:4 to be accurate). This provides a smoother motion of the slider compared to 2:1 and 3:1 ratios [36]. Table 2 shows the design parameters for six different B-LVCM devices. The difference between SHORT and LONG devices is their stator/slider length. As mentioned before, the B-LVCM is a long-range micropositioner, which is a direct benefit of microball-bearing mechanism. The range of motion is defined by the length of the identical separate trenches on the stator. As shown in table 2, the range of motion can be from 3 mm up to about 6 mm.

Figure 1(*b*) shows the B-LVCM principle of operation. The device can be driven by six square-wave voltages in the

Table 2. Six different designs of the B-LVCM.

Device	Air gap (μm)	Electrode width/pitch (μm)	Pole width/pitch (μm)	Active area (mm^2)	Range of motion (mm)
$D1_{SHORT}$	5	30/40	30/60	31.05	3.86
$D1_{LONG}$	5	30/40	30/60	50.25	5.78
$D2_{SHORT}$	10	90/120	90/180	31.95	3.66
$D2_{LONG}$	10	90/120	90/180	49.95	5.82
$D3_{SHORT}$	20	180/240	180/360	35.10	3.00
$D3_{LONG}$	20	180/240	180/360	49.50	5.88

form of a complementary 6-phase configuration, where A, B and C are 120° out of phase, and D, E and F are the inverse of A, B and C, respectively. When the excitation voltage is applied to stator electrodes, image charges are induced on the slider poles. The resulting electrostatic force aligns the active electrodes and poles, leading to slider motion. Continuous motion of the slider is achieved by exciting all six phases in the appropriate sequence. The direction of the slider motion can be changed by switching the excitation order of two complementary phase pairs (e.g. A/D and B/E).

Assuming the slider to be the potential reference, the B-LVCM can be modeled as a multiconductor system with six conductors (representing six phases). This system can be defined by a 6×6 capacitance matrix, which can be shown as (assuming negligible end effects and considering the symmetry of the device structure)

$$\bar{C} = \begin{bmatrix} C_{ph} & C_1 & C_2 & C_3 & C_2 & C_1 \\ C_1 & C_{ph} & C_1 & C_2 & C_3 & C_2 \\ C_2 & C_1 & C_{ph} & C_1 & C_2 & C_3 \\ C_3 & C_2 & C_1 & C_{ph} & C_1 & C_2 \\ C_2 & C_3 & C_2 & C_1 & C_{ph} & C_1 \\ C_1 & C_2 & C_3 & C_2 & C_1 & C_{ph} \end{bmatrix}$$

where C_{ph} is the self-capacitance of each phase, and C_1, C_2 and C_3 are the mutual capacitances. The energy stored in the system is a function of phase potentials and slider potential, which is determined by the capacitance matrix. It can be shown that in the case of a complementary 6-phase excitation, the slider potential is zero as a result of the symmetry. Based on the above assumptions and assuming that only the diagonal elements of the capacitance matrix vary with the position of the slider, a first-order approximation of the aligning force generated by each phase can be written as

$$F_{ph} = \frac{1}{2} V_{ph}^2 \frac{\partial C_{ph}}{\partial x} \tag{1}$$

where V_{ph} is the amplitude of the excitation voltage, C_{ph} is the B-LVCM capacitance per phase, and x is the position of the slider.

Table 3 shows the estimated maximum aligning force for the six B-LVCM designs, assuming a minimum capacitance of zero and a linear profile for the spatial gradient of the capacitance. The instantaneous aligning force is a function of the slider position. The maximum capacitance was numerically calculated using FEMLAB^{TM}. For each phase, the maximum capacitance occurs when all the stator electrodes of that phase are fully aligned with a set of slider poles. The minimum capacitance occurs when there is no overlap between the stator electrodes of that phase and any of the slider poles.

Table 3. Estimated force and speed of the B-LVCM.

	Maximum aligning force at 100 V P-P (mN)		Average slider speed (mm s^{-1})		
Device	Per phase	Total (six phases)	10 Hz	20 Hz	50 Hz
$D1_{SHORT}$	1.02	3.07	0.6	1.2	3.0
$D1_{LONG}$	1.61	4.82	0.6	1.2	3.0
$D2_{SHORT}$	0.20	0.59	1.8	3.6	9.0
$D2_{LONG}$	0.31	0.93	1.8	3.6	9.0
$D3_{SHORT}$	0.05	0.14	3.6	7.2	18.0
$D3_{LONG}$	0.08	0.23	3.6	7.2	18.0

Table 4. Control parameters of the B-LVCM.

Output parameter	Control parameter
Aligning force	Amplitude of excitation voltage
Slider speed	Frequency of excitation voltage
Direction of motion	Excitation order of phase pairs

Since the B-LVCM is a synchronous machine, assuming a 50% duty cycle for the excitation waveforms, the average slider speed in steady-state continuous motion can be written as

$$u_{ave} = 2Wf_s \tag{2}$$

where W is the electrode/pole width and f_s is the frequency of the stator excitation. The estimated average slider speed is also shown in table 3.

The important output parameters of the B-LVCM, as shown in table 4, are the average aligning force applied to the slider, the average speed of the slider motion and the direction of motion. For a designed B-LVCM there are certain parameters that can be changed for controlling the B-LVCM. These parameters can be used in both open-loop and closed-loop control configuration. We have used an open-loop configuration to control the B-LVCM. However, the open-loop control has a limited range of operation and a closed-loop control, which includes position sensors and active control of the excitation voltages, is especially necessary for micropositioning applications. It should be noted that with an open-loop control the precision of positioning is essentially determined by the electrode pitch and is affected by the irregularities due to fabrication tolerances. With a closed-loop control, however, the accuracy of the position sensor determines the precision of the positioning. As long as the control of a static parameter, e.g. position, is concerned, the nonuniformities of friction do not affect the precision of the positioning. However, in controlling the dynamic parameters, e.g. speed and force, the friction profile of the bearing has to be taken into account.

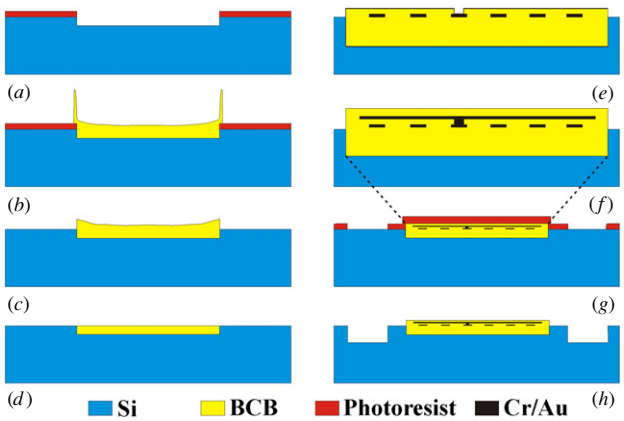

Figure 2. Process steps for fabrication of the stator: (*a*) pattern and etch Si pit with DRIE, (*b*) spin-cast and pattern photo-BCB, (*c*) lift off BCB ridges, (*d*) planarize EBiS island with CMP, (*e*) fabricate Cr/Au interconnections and pattern photo-BCB to open vias, (*f*) fabricate Cr/Au electrodes and pattern photo-BCB passivation layer, (*g*) pattern and (*h*) etch trenches with DRIE.

4. Linear micromotor fabrication

Fabrication of the stator included eight photolithography steps summarized in three stages: (1) development of EBiS islands, (2) fabrication of a two-level metal interconnection/electrode structure and (3) fabrication of the microball housings. All BCB depositions were performed using spin-on photosensitive BCB according to an in-house photosensitive BCB process. As shown in figures 2(*a*)–(*d*), a 25 μm deep planarized EBiS island was fabricated using photolithography, deep reactive ion etching (DRIE) and chemical mechanical planarization (CMP) [11]. The degree of planarization of EBiS islands affects the subsequent processes and is critical in the performance of the device. Previously, we showed that a planarization of more than 95% was achieved using the EBiS process [11]. The interconnections and electrodes consisting of 20 nm thick chromium (Cr) and 200 nm thick gold (Au) films were fabricated on top of the EBiS islands using sputtering and lift-off, as shown in figures 2(*e*) and (*f*). A BCB ILD layer was fabricated to isolate interconnections and electrodes. The ILD layer incorporated several vias that were used to interconnect the two metal levels wherever required. Another BCB layer (passivation) was fabricated to protect the active area. Finally, the microball housings were etched in the stator using DRIE, as shown in figures 2(*g*) and (*h*). The average etch depth of the trenches across the stator wafer was measured to be 125.2 μm with a standard deviation of 0.2%, which indicates good uniformity of the microball housing depth on the stator wafer. Figure 3 shows a complete fabricated stator of device $D2_{SHORT}$ with four microballs placed in the trenches. The fabrication yield of the stator of device $D2_{SHORT/LONG}$ was better than other devices; therefore, all tests presented in this paper were performed on device $D2_{SHORT/LONG}$.

Fabrication of the slider included one standard photolithography step and one DRIE step. Figure 4 shows a complete fabricated slider with two microballs placed in the trenches. Note that what is shown in figure 4 is the bottom of the slider in an assembled B-LVCM. Both microball housings and the slider poles were etched to the same approximate depth. The height of the slider poles is trivial as long as it is much larger than the air gap and the electrode/pole width. However, the depth of the housings is important since it defines the air gap. The average etch depth of the trenches across the slider wafer was measured to be 142.6 μm with a standard deviation of 3.3%, which is significantly higher compared to that of the stator trenches. This is believed to be caused by the high loading of the slider wafer during DRIE since a large portion of silicon was exposed to the plasma. For the experiments on device $D2_{SHORT}$, we diced the wafer into pieces and picked a slider with an average etch depth of 144.6 μm and standard deviation of 1.3%. This defines an air gap with an average of 15.2 μm and a standard deviation of 12.6%, which corresponds to a variation of 1.9 μm across the device. Similarly, for experiments on device $D2_{LONG}$ an average air gap of 19.2 μm was used.

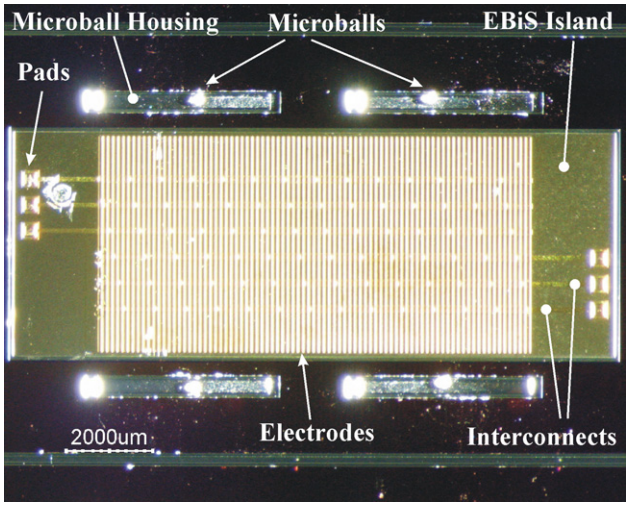

Figure 3. Top view of a fabricated stator (device $D2_{SHORT}$) with four microballs placed in bearing housings.

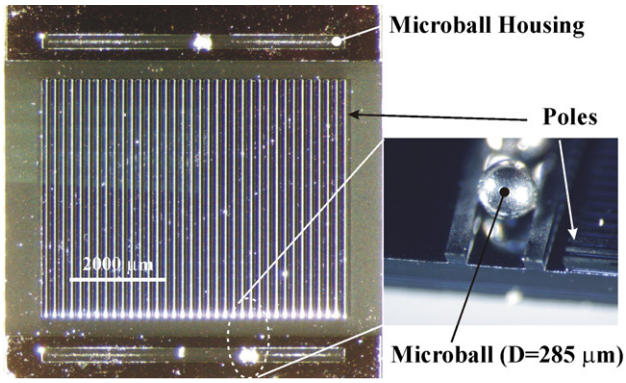

Figure 4. Top view of a fabricated slider (device $D2_{SHORT}$) with two microballs placed in bearing housings.

5. Linear micromotor characterization

The primary output parameters that can characterize the behavior of the B-LVCM in steady-state operation are the instantaneous aligning force and slider speed. We measured these quantities indirectly by measuring the capacitance and

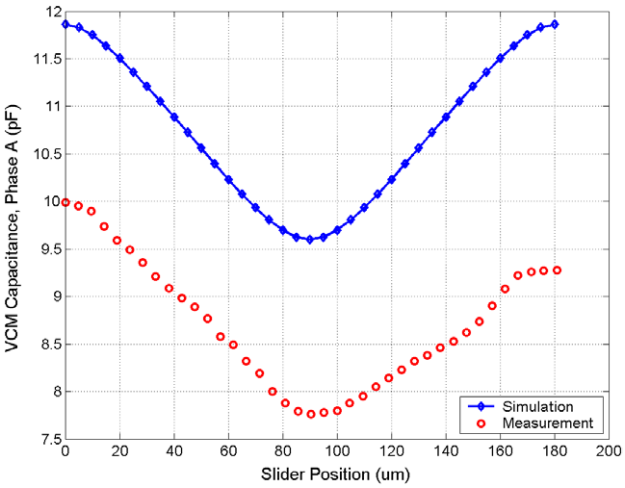

Figure 5. Simulated and measured B-LVCM capacitances for device D2 $_{\mathrm{SHORT}}$.

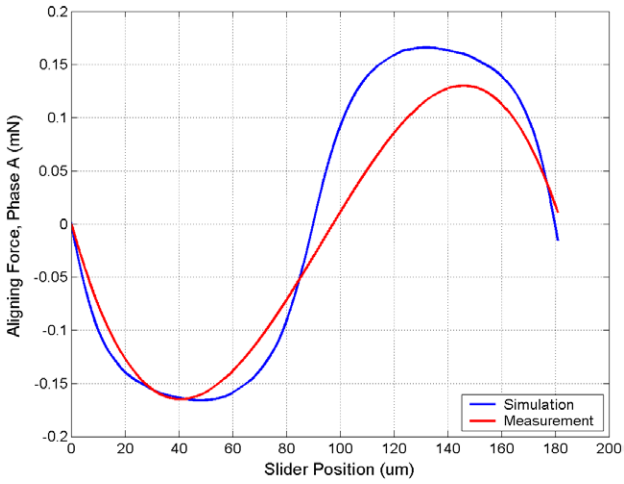

Figure 6. Simulated and extracted (from capacitance data) B-LVCM aligning force for device $D2_{\mathrm{SHORT}}$ when excited with a 100 V dc voltage. The force was calculated from curve fits to the simulated and measured capacitance data of figure 5.

the slider position. As equation (1) shows, the force is proportional to the spatial gradient of the capacitance, therefore, by measuring the capacitance of the B-LVCM, we can extract the aligning force as a function of slider position. Similarly, since the speed is the time derivative of the position, by measuring the position of the slider, we can obtain the speed of the slider as a function of time (or slider position).

Figure 5 shows the simulated and measured capacitance profile of *phase A* as a function of the slider position for device $D2_{\mathrm{SHORT}}$. Since the profile is periodic with the position, only one period is shown. The reference point (zero) of the slider position is the maximum capacitance position, where phase A electrodes are fully aligned with the corresponding slider poles. The simulated profile was numerically calculated using FEMLAB$^{\mathrm{TM}}$ with the slider shifted in 5 μm steps. The measured profile was obtained by manually moving the slider in 5 μm steps using a probe needle micropositioner and measuring the capacitance between the slider and phase A using a capacitance meter. The position of the slider was measured using a microscope. There is good agreement between the general trends of the two profiles; however, the 20% difference between the absolute values of the measured and simulated capacitances can be explained in terms of tolerances in the fabrication of the trenches, electrodes, poles, the non-uniformity of etch across the device and fabrication defects. In addition, during the simulation all non-active phases were connected to ground, while during the measurement, all non-active phases were floated. However, in extraction of the force from capacitance only the slope of the graph is important and the absolute values do not contribute to the outcome.

Using equation (1) and assuming a 100 V dc excitation voltage, the aligning force as a function of the slider position was extracted from the simulated and measured capacitance data after a cubic polynomial curve fit (figure 6). There is good agreement between the aligning force profiles extracted from simulated and measured data. The maximum aligning force for both profiles is 0.17 mN, close to the estimated value of 0.20 mN from table 3.

Figure 7 shows similar profiles for all six phases of device $D2_{\mathrm{LONG}}$ with an estimated air gap of 19.2 μm. The

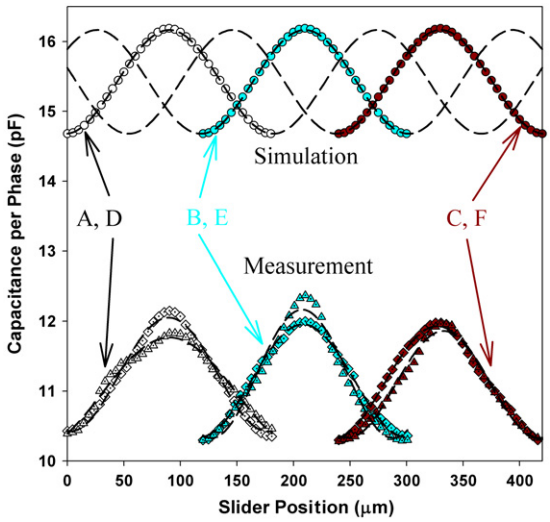

Figure 7. Simulated and measured capacitances of all six B-LVCM phases for device $D2_{\mathrm{LONG}}$. The data are fit to sine-squared functions.

total aligning force profiles calculated from the capacitance profiles (after a sine-squared curve fit and assuming a 6-phase configuration with 100 V P-P excitation voltage) are shown in figure 8. There is good agreement between the simulation and measurement average force (0.24 mN versus 0.27 mN). The maximum simulated aligning force is 0.25 mN, while the maximum measured aligning force is 0.41 mN. The discrepancy between these data and table 3 is due to the difference between designed and fabricated air gap. Furthermore, the effect of fringing electric field was neglected in calculating the data in table 3.

Although the above method is an indirect measurement of the aligning force, equation (1) can predict the aligning force of a 6-phase micromotor fairly accurately and the only major limitation is the relative error in the measurement of the capacitance. Direct measurement of the applied force to a moving slider in an operational micromotor without disturbing the motion of the slider is practically impossible. One approach to directly measure the force is to redesign

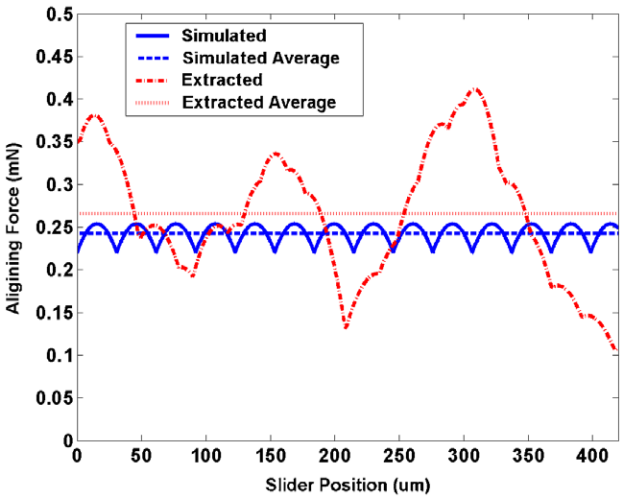

Figure 8. Simulated and extracted total aligning force and their average values for device $D2_{LONG}$ when excited with a 100 V P-P voltage. The force is calculated from curve fits to the simulated and measured capacitance data of figure 7.

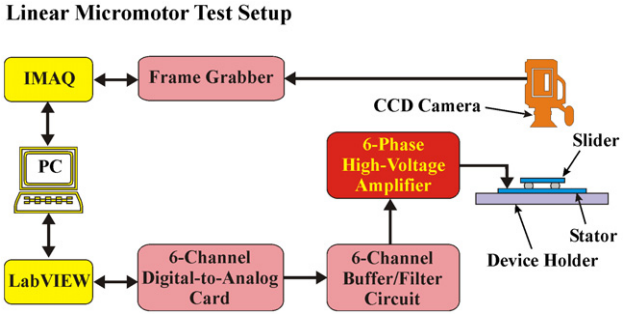

Figure 9. Experimental setup for driving the B-LVCM and characterization of the slider motion.

the motor to incorporate tethers and force sensors in the slider, which ultimately leads to an even more complicated fabrication process.

An experimental setup, shown in figure 9, was designed and built to drive the B-LVCM with AC excitation voltages in multiphase configuration and characterize the motion of the slider. The drive parameters were controlled by a LabVIEW program. The motion of the slider was captured by a commercial camcorder at 30 frames s^{-1}. IMAQ Vision Builder software controlled the camera and captured the frames. IMAQ was also used to post-process the captured images of the slider and track a mark placed on the slider to extract the position of the slider as a function of time. This is similar to the method we previously used to characterize the dynamic friction of microball bearings [4].

The initial AC tests of the B-LVCM were performed with a 3-phase configuration, where only three phases A, B and C were excited with square-wave voltages, and phases D, E and F were floating. The phase differences between A, B and C were 120°, similar to the 6-phase configuration. Figure 10 shows the position of the slider as a function of time when device $D2_{SHORT}$ was driven at 10 Hz and 100 V P-P. The direction of the motion was switched at 2 Hz to obtain a periodic motion.

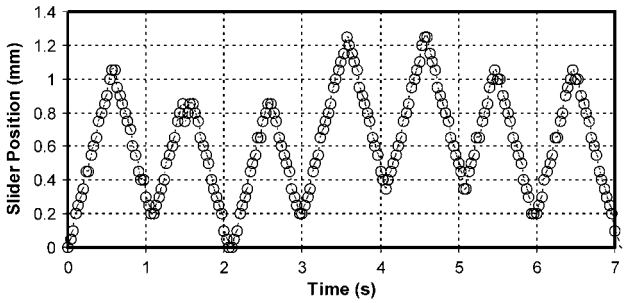

Figure 10. Measured slider position versus time for device $D2_{SHORT}$ when excited with a 3-phase, 10 Hz, 100 V P-P, square-wave voltage (direction was changed at 2 Hz).

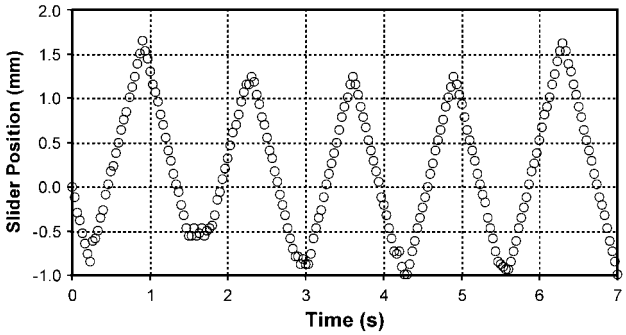

Figure 11. Measured slider position versus time for device $D2_{SHORT}$ when excited with a 6-phase, 20 Hz, 120 V P-P, square-wave voltage (direction was changed at 1.5 Hz).

Table 5. Estimated and measured average speed for device $D2_{SHORT}$ when excited with a 6 phase, 120 V P-P, square-wave voltage at different excitation frequencies.

Excitation frequency (Hz)	Estimated average speed (mm s^{-1})	Measured average speed (mm s^{-1})
10	1.80	1.94 ± 0.02
20	3.60	3.98 ± 0.02
40	7.20	7.37 ± 0.12
80	14.40	7.21 to 11.10

A drift in the center position was observed that is believed to be due to the non-uniformity of the air gap. The average speed calculated over the slopes of the graph in figure 10 was 1.82 mm s^{-1}, within 1.1% of the theoretical value (1.80 mm s^{-1} from table 3).

As seen in figure 10, the motion of the slider in each ramp is not smooth and exhibits some irregularities, i.e. the data points are not equally distant on the position axis. This means that the instantaneous slider speed undergoes sudden changes at times. A similar experiment at 20 Hz with a switching frequency of 4 Hz resulted in an average speed of 3.56 mm s^{-1}, again within 1.1% of the theoretical value (3.60 mm s^{-1} from table 3) and with similar irregularities in the slider motion.

It was expected that a smoother slider motion would be achievable if a 6-phase configuration was used. In order to verify this, the ac test with a 6-phase configuration was performed on device $D2_{SHORT}$. Figure 11 shows the position of the slider as a function of time for the device driven at 20 Hz and 120 V P-P. The average speed was 3.98 mm s^{-1}, within 10.5% of the theoretical value (3.60 mm s^{-1} from

table 3). Figure 11 shows a much smoother slider motion in each ramp compared to figure 10. A similar experiment at 10 Hz resulted in an average speed of 1.94 mm s^{-1}, within 7.7% of the theoretical value (1.80 mm s^{-1} from table 3). Table 5 shows the estimated and measured average speeds at different frequencies for a 6-phase configuration. Note that the motor is not able to synchronize at higher frequencies, e.g. 80 Hz. This inability is a consequence of the open-loop control scheme used for operating the device, as opposed to a fundamental characteristic. There is no appreciable difference between 3-phase and 6-phase configurations as far as the average speed is concerned, although, as described before, a visual observation verifies that the 6-phase configuration provides smoother motion as expected.

6. Conclusion

In this paper, we presented the design, fabrication and characterization of a microball-bearing-supported, bottom-drive, linear, variable-capacitance micromotor using benzocyclobutene polymer films as insulating layers. The successful development of the micromotor is the first demonstration of a microelectromechanical device using microball bearing and benzocyclobutene polymer technologies. This device was fabricated on the basis of the embedded benzocyclobutene in silicon process. The micromotor was successfully operated and characterized with 3-phase and 6-phase drive configurations. A smoother slider motion was achieved using a 6-phase drive configuration. The capacitance, aligning force and slider speed were numerically calculated and experimentally measured. A comparison of the theoretical and experimental results showed that the micromotor operates as predicted with a deviation mainly attributed to fabrication imperfections. An electromechanical model is being developed that can accurately predict the transient and steady-state operation of the device. The transient operation of the device is being studied using a high-speed camera. The linear micromotor can operate as a long-range, high-speed micropositioner. It can also be used as a technology platform to develop microball-bearing-supported rotary micromotors and microgenerators.

Acknowledgements

This work is supported by the National Science Foundation (NSF) under grant no. ECS-0224361, the Army Research Office (ARO) through MAV MURI Program under grant no. ARMY-W911NF0410176 with Technical Monitor Dr Tom Doligalski, and the Army Research Lab (ARL) under CA no. W911NF-05-2-0026. The authors would like to thank Nitta Haas Company, Japan for supplying the ILD1300 slurry. We would also like to thank Mr Thomas C Loughran and Mr Nolan A Ballew from University of Maryland for help with fabrication.

References

[1] Ghodssi R, Denton D D, Seireg A A and Howland B 1993 Rolling friction in a linear microactuator *J. Vac. Sci. Technol.* A **11** 803–7

[2] Mills M E, Townsend P, Castillo D, Martin S and Achen A 1997 Benzocyclobutene (DVS-BCB) polymer as an interlayer dielectric (ILD) material *Microelectron. Eng.* **33** 327–34

[3] Modafe A, Ghalichechian N, Frey A, Lang J H and Ghodssi R 2005 A microball-bearing-supported linear electrostatic micromotor with benzocyclobutene polymer insulating layers *Proc. 13th Int. Conf. on Solid-State Sensors, Actuators, and Microsystems (Transducers '05) (Seoul, Korea)* pp 693–6

[4] Lin T W, Modafe A, Shapiro B and Ghodssi R 2004 Characterization of dynamic friction in MEMS-based microball bearings *IEEE Trans. Instrum. Meas.* **53** 839–46

[5] Tan X, Modafe A and Ghodssi R 2005 An empirical model for dynamic friction in microfabricated linear microball bearings *Proc. 24th American Control Conf. (ACC 2005) (Portland, OR)* pp 2463–8

[6] Tan X, Modafe A and Ghodssi R 2005 Modeling of velocity-dependent rolling friction in linear microball bearings *Proc. ASME World Tribology Congress III (WTC2005) (Washington, DC)*

[7] Tan X, Modafe A, Hergert R, Ghalichechian N, Shapiro B, Baras J S and Ghodssi R 2004 Vision-based microtribological characterization of linear microball bearings *Proc. ASME/STLE Int. Joint Tribology Conf.: Special Symposia on Contact Phenomena in MEMS (TRIB2004) (Long Beach, CA)* pp 23–8

[8] Ghalichechian N, Modafe A, Ghodssi R, Lazzeri P, Micheli V and Anderle M 2004 Integration of benzocyclobutene polymers and silicon micromachined structures using wet anisotropic etching *J. Vac. Sci. Technol.* B **22** 2439–47

[9] Modafe A, Ghalichechian N and Ghodssi R 2005 Multilevel interconnection and isolation for electrostatic MEMS using embedded benzocyclobutene in silicon process (invited paper) *Proc. 22nd Int. VLSI/ULSI Multilevel Interconnection Conf. (2005 VMIC) (Fremont, CA)*

[10] Modafe A, Ghalichechian N, Kleber B and Ghodssi R 2004 Electrical characterization of benzocyclobutene polymers for electric micromachines *IEEE Trans. Device Mater. Reliab.* **4** 495–508

[11] Modafe A, Ghalichechian N, Powers M, Khbeis M and Ghodssi R 2005 Embedded benzocyclobutene in silicon: an integrated fabrication process for electrical and thermal isolation in MEMS *Microelectron. Eng.* **82** 154–67

[12] Fan L-S, Tai Y-C and Muller R S 1988 Integrated movable micromechanical structures for sensors and actuators *IEEE Trans. Electron Devices* **35** 724–30

[13] Mehregany M, Gabriel K J and Trimmer W S N 1988 Integrated fabrication of polysilicon mechanisms *IEEE Trans. Electron Devices* **35** 719–23

[14] Frechette L G, Jacobson S A, Breuer K S, Ehrich F E, Ghodssi R, Khanna R, Wong C W, Zhang X, Schmidt M A and Epstein A H 2000 Demonstration of a microfabricated high-speed turbine supported on gas bearing *Proc. Solid-State Sensor and Actuator Workshop (Hilton Head Island, SC)* pp 43–7

[15] Bart S F 1990 Modeling and design of electrostatic actuators *PhD Dissertation Thesis* Department of Electrical Engineering and Computer Science, Massachusetts Institute of Technology, Cambridge, MA, USA

[16] Nagle S F, Livermore C, Frechette L G, Ghodssi R and Lang J H 2005 An electric induction micromotor *J. Microelectromech. Syst.* **14** 1127–43

[17] Genda T, Tanaka S and Esashi M 2003 High power electrostatic motor and generator using electrets *Proc. 12th Int. Conf. on Solid State Sensors, Actuators and Microsystems (Transducers '03) (Boston, MA, USA)* pp 492–5

[18] Makin B and Coles B J 1993 Novel electrostatic micromotors *Proc. 6th Int. Conf. on Electrical Machines and Drives (Oxford, UK)* pp 1–3

[19] Akiyama T and Fujita H 1995 A quantitative analysis of scratch drive actuator using buckling motion *Proc. IEEE Micro Electro Mechanical Systems (MEMS'95) (Amsterdam, The Netherlands)* pp 310–5
[20] Baginsky I L and Kostsov E G 2003 High-energy capacitance electrostatic micromotors *J. Micromech. Microeng.* **13** 190–200
[21] Bexell M and Johansson S 1999 Fabrication and evaluation of a piezoelectric miniature motor *Sensors Actuators* A **75** 8–16
[22] Robert P, Danel J S and Villard P 1997 The electrostatic ultrasonic micromotor *J. Micromech. Microeng.* **7** 170–2
[23] Epstein A H 2004 Millimeter-scale, micro-electro-mechanical systems gas turbine engines *Trans. ASME, J. Eng. Gas Turbines Power* **126** 205–26
[24] Epstein A H *et al* 1997 Power MEMS and microengines *Proc. 9th Int. Conf. on Solid-State Sensors and Actuators (Transducers'97) (Chicago, IL, USA)* pp 753–6
[25] Chen K-S, Chen J-Y and Lin S-Y 2002 Fracture analysis of thick plasma-enhanced chemical vapor deposited oxide films for improving the structural integrity of power MEMS *J. Micromech. Microeng.* **12** 714–22
[26] Chen K-S, Zhang X and Spearing S M 2001 Processing of thick dielectric films for power MEMS: stress and fracture *Proc. MRS Materials Science of Microelectromechanical Systems (MEMS) III Symp. (Warrendale, PA, USA)* vol 657, pp EE8.4.1–6
[27] Ghodssi R, Frechette L G, Nagle S F, Zhang X, Ayon A A, Senturia S D and Schmidt M A 1999 Thick buried oxide in silicon (TBOS): an integrated fabrication technology for multi-stack wafer-bonded MEMS processes *Proc. 10th Int. Conf. on Solid-State Sensors and Actuators (Tansducers'99) (Sendai, Japan)* pp 1456–9
[28] Zhang X, Chen K-S, Ghodssi R, Ayon A A and Spearing S M 2001 Residual stress and fracture in thick tetraethylorthosilicate (TEOS) and silane-based PECVD oxide films *Sensors Actuators* A **91** 373–80
[29] Zhang X, Chen K-S and Spearing S M 2003 Thermo-mechanical behavior of thick PECVD oxide films for power MEMS applications *Sensors Actuators* A **103** 263–70
[30] Zhang X, Ghodssi R, Chen K-S, Ayon A A and Spearing S M 2000 Residual stress characterization of thick PECVD TEOS film for power MEMS applications *Proc. Solid-State Sensor and Actuator Workshop (Hilton Head Island, SC, USA)* pp 316–9
[31] Raieszadeh M, Monajemi P, Yoon S-W, Laskar J and Ayazi F 2005 High-*Q* integrated inductors on trenched silicon islands *Proc. 18th Int. Conf. on Micro Electro Mechanical Systems (MEMS '05) (Miami, FL)* pp 199–202
[32] Barillaro G, Diligenti A, Nannini A and Pennelli G 2003 A thick silicon dioxide fabrication process based on electrochemical trenching of silicon *Sensors Actuators* A **107** 279–84
[33] Zhang C and Najafi K 2004 Fabrication of thick silicon dioxide layers for thermal isolation *J. Micromech. Microeng.* **14** 769–74
[34] Chou T-K A and Najafi K 2001 3D MEMS fabrication using low-temperature wafer bonding with benzocyclobutene (BCB) *Proc. 11th Int. Conf. on Solid-State Sensors and Actuators (Transducers'01) (Munich, Germany)* pp 1570–3
[35] Guo S 2003 Cyclotene(R) diaphragm for MEMS-based IR detectors *Proc. SPIE Micromachining and Microfabrication Process Technology VII Conf. (San Jose, CA, USA)* pp 422–9
[36] Mehregany M, Bart S F, Tavrow L S, Lang J H and Senturia S D 1990 Principles in design and microfabrication of variable-capacitance side-drive motors *J. Vac. Sci. Technol.* A **8** 3614–24